www.acsnano.org

Dual Atomic Coherence in the Self-Assembly of Patchy Heterostructural Nanocrystals

Hua Zhu, Zhaochuan Fan, Siyuan Song, Dennis Eggert, Yuzi Liu, Wenwu Shi, Yucheng Yuan, Kyung-Suk Kim, Michael Grünwald,* and Ou Chen*



Downloaded via BROWN UNIV on September 11, 2022 at 20:35:15 (UTC). See https://pubs.acs.org/sharingguidelines for options on how to legitimately share published articles.

Cite This: https://doi.org/10.1021/acsnano.2c06167



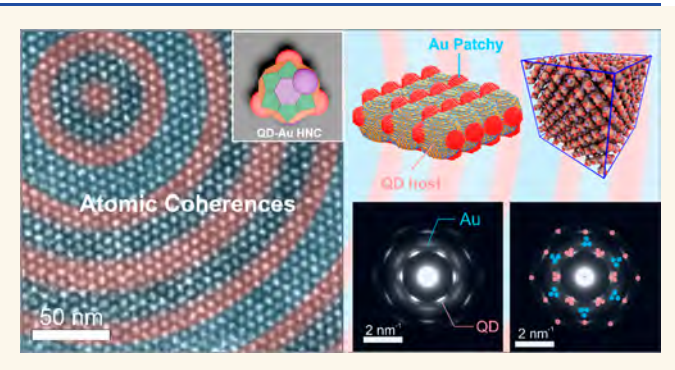
ACCESS I

III Metrics & More

Article Recommendations

Supporting Information

ABSTRACT: Advances in the synthesis and self-assembly of nanocrystals have enabled researchers to create a plethora of different nanoparticle superlattices. But while many superlattices with complex types of translational order have been realized, rotational order of nanoparticle building blocks within the lattice is more difficult to achieve. Self-assembled superstructures with atomically coherent nanocrystal lattices, which are desirable due to their exceptional electronic and optical properties, have been fabricated only for a few selected systems. Here, we combine experiments with molecular dynamics (MD) simulations to study the self-assembly of heterostructural nanocrystals (HNCs), consisting of a near-spherical quantum



dot (QD) host decorated with a small number of epitaxially grown gold nanocrystal (Au NC) "patches". Self-assembly of these HNCs results in face-centered-cubic (fcc) superlattices with well-defined orientational relationships between the atomic lattices of both QD hosts and Au patches. MD simulations indicate that the observed dual atomic coherence is linked to the number, size, and relative positions of gold patches. This study provides a strategy for the design and fabrication of NC superlattices with large structural complexity and delicate orientational order.

KEYWORDS: self-assembly, superlattice, quantum dot, heterostructural nanocrystals, atomic coherence, electron diffraction

INTRODUCTION

Self-assembly of inorganic nanocrystals (NCs) into superlattices (SLs) is a powerful strategy for incorporating the tailorable properties of nanoparticles into functional nanomaterials. 1-8 A wide range of NCs with different sizes, shapes, and compositions has been self-assembled into highly ordered superstructures with continuously improved structural diversity and complexity, along with exceptional properties that are inaccessible to either discrete NCs or less ordered aggregates. 9-40 The vast majority of assembled SLs are composed of NCs that are well ordered translationally but disordered with respect to the relative orientations of constituent NC atoms. 1,2 In contrast, it has been demonstrated in both experimental studies and theoretical calculations that atomic coherent NC-SLs with NC lattice orientation alignments possess unique and promising properties that are missing from atomically disordered SLs. 41-44 For instance, epitaxially connected SLs of quantum dots (QDs) can display a near-complete delocalization of charge carriers⁴² and give rise to quantum phenomena such as Dirac cones and topological states. 41 As another example, the generation of superfluorescent light has been recently reported in self-assembled CsPbBr₃ perovskite QD nanocubes with a high level of atomic

coherences. Although promising, the fabrication of such superstructures with atomic orientational orderings remains extremely challenging. This is because many types of NCs interact isotopically and lack the highly directional interactions required to regulate underlying atomistic lattices of the NC building blocks. We recently reported the control and tuning of NC orientation and atomic coherence using a class of NC building blocks: hybrid QD-metal heterostructural NCs (HNCs). The interactions between HNCs can be modulated via the placement of metal patches (i.e., small Au NCs), as well as the chemical identity and population of ligands on HNC surfaces. However, the observed atomic lattice alignment was limited to the QD crystalline host. Achieving atomic lattice coherences across different crystalline components of HNCs has yet to be reported.

Received: June 22, 2022 Accepted: August 29, 2022



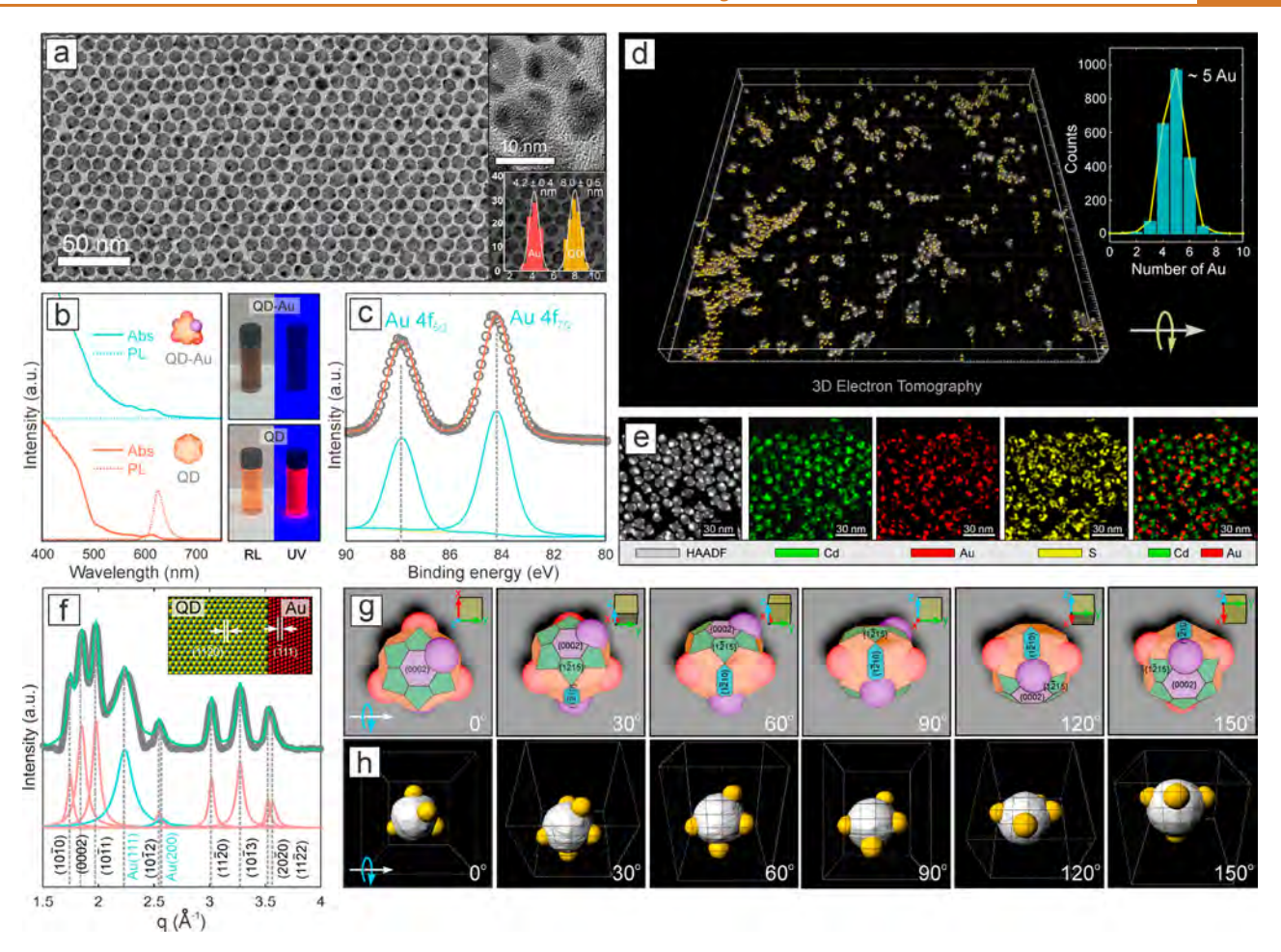


Figure 1. Characterizations of QD-Au HNCs. (a) Representative TEM image showing the as-synthesized HNCs. (b) (left) UV—vis and PL spectra QD (bottom) and QD-Au HNC (top) samples. (right) photographs of QD and QD-Au HNC samples under room light and UV irradiation. (c) XPS spectrum of the QD-Au HNCs showing two characteristic peaks of Au^0 ($4f_{7/2}$ and $4f_{5/2}$). (d) Snapshot from a large-area 3D electron tomography movie. Inset: number distribution of Au patches per QD. (e) HAADF-STEM and elemental mapping for Cd, Au, and S of HNCs. (f) XRD pattern of QD-Au HNCs (gray), fitted curve (green), and constituent peaks (pink and blue). (g, h) Proposed 3D geometric model (top row) and snapshots from an electron tomography measurement (bottom row) for a single HNC at different rotating angles.

In this paper, we report the synthesis and self-assembly of a family of QD-Au HNCs, consisting of a near-spherical QD host epitaxially decorated with a small number (~5) of Au patches on the HNC surfaces. Unlike previous studies, the Au patches are large enough to not only influence assembly behavior of HNC but also allow probing of relative atomic orientations of Au patches in the final HNC-SLs. Upon solvent evaporation, QD-Au HNCs assemble into a face-centeredcubic (fcc) SL. A high level of atomic alignment among QD hosts and Au patches was observed due to the epitaxy between these two constituents. Combining real and reciprocal space characterization techniques, we have determined the orientational relations of both QD and Au lattices with high accuracy. Molecular dynamics (MD) computer simulations of a coarsegrained HNC model reveal that the orientational order of HNCs is induced by the strong tendency of Au patches to occupy the natural voids in the fcc SL. The number, relative positions, and size of Au patches are all crucial to the orientational order observed. Our study not only demonstrates a different strategy to fabricate self-assembled multicomponent hybrid nanomaterials with structural control at the atomic level but also sheds light on understanding self-assembly behaviors of patchy particles at different length scales in general.

RESULTS AND DISCUSSION

"Patchy" epitaxially grown QD-Au HNC building blocks. We synthesized CdSe-CdS core-shell QD with epitaxially grown Au patches using a modified version of our previously reported method.^{35,47} Specifically, we found that a careful control of the heating rate is essential to achieve stable Au patches with appreciable sizes (see details in the Supporting Information). Transmission electron microscope (TEM) images showed narrow size distributions for both QD hosts and Au patches, with diameters of 8.0 ± 0.5 and 4.2 ± 0.4 nm, respectively (Figure 1a and Figures S1 and S2). The noticeable increase in the UV-vis absorption (from plasmonic resonance of Au patches) of the final QD-Au HNCs strongly supported the growth of Au patches on the surface of QD hosts (Figure 1b). In addition, the photoluminescence (PL) spectrum showed a complete "quenching" behavior upon Au growth, due to the enhanced charge separation induced by epitaxial attachment of Au patches on semiconductor QDs. 47photoelectron spectroscopy (XPS) measurements showed two characteristic peaks of Au⁰ centered at 84.1 eV (4f_{7/2}) and 87.8 eV $(4f_{5/2})$ (Figure 1c), consistent with TEM and optical measurement results.⁵⁰ We used three-dimensional (3D)

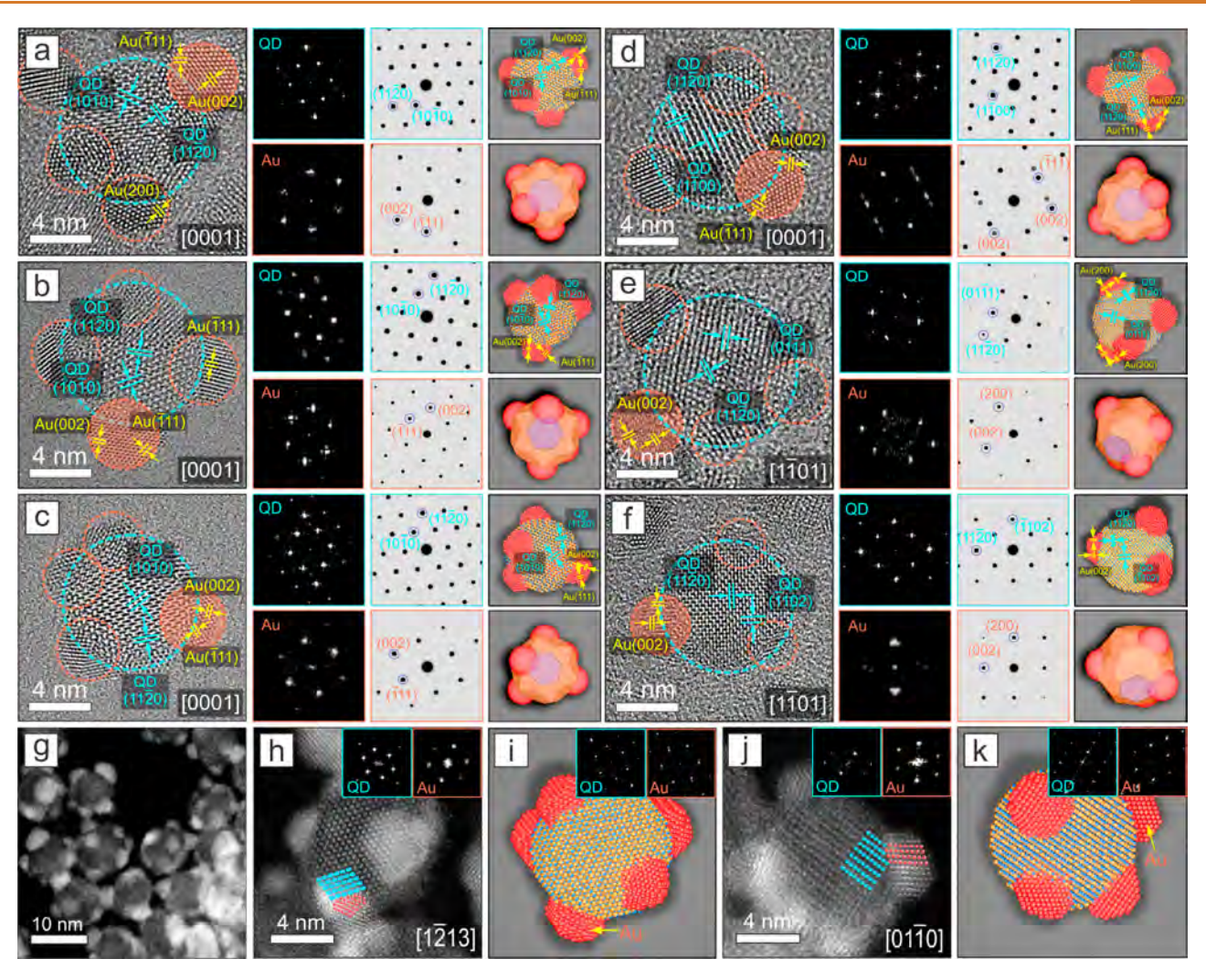


Figure 2. Characterizations of single QD-Au HNCs. (a-f) Characterization of HNC geometry and crystal growth at different viewing directions using bright-field HR-TEM. (left) HR-TEM images of single HNCs viewed along different crystallographic directions of the QD. (right) Fast Fourier transform (FFT) patterns of the HR-TEM image for the QD (top left) and Au (bottom left) crystalline domains, computer-simulated ED patterns (middle), 3D HNC atomistic models (top right), and 3D polyhedral HNC model (bottom right, {0002}_{QD} facet of the QD host is highlighted in purple) viewed from the corresponding direction. (g) Representative HAADF-STEM image of QD-Au HNCs. (h, j) HAADF-STEM images of a single HNC from different viewing directions. Inset: corresponding FFT patterns of QD (blue) and Au (red) crystalline domains. (i, k) Corresponding 3D atomistic models and simulated FFT patterns of QD (blue) and Au (red, from the Au patch indicated by a yellow arrow) crystalline domains.

electron tomography to count the number of Au patches on over 2000 particles; HNCs with 5 Au patches make up the largest population, but significant numbers of HNCs with four or six patches were also observed (Figure 1d and Movie S1). The QD-Au hybrid composition of HNCs was further confirmed by high-angle annular dark-field (HAADF) scanning TEM (STEM) imaging and elemental mapping (Figure 1e). Powder X-ray diffraction (XRD) showed that the wurtzite (WZ) crystal structure of the CdSe-CdS core-shell QDs remained intact after Au growth (Figure 1f), whereas the additional broad diffraction peak centered at $q = 2.24 \text{ Å}^{-1}$ can be assigned to the Bragg diffraction of Au (111) planes (Figure 1f). The calculated d spacing of 2.80 Å indicated a large lattice expansion of ~19% compared to bulk Au (in line with previous reports³⁵), suggesting epitaxial growth of Au patches on the surface of QDs (Figure 1f and Table S1). Our previous study showed that small Au NC patches would preferentially grow on $\{1210\}_{QD}$ and $\{1215\}_{QD}$ facets of WZ core-shell QDs, in which Au patches can possibly minimize the large interfacial

strain generated by the lattice mismatch between QD and Au. Based on this growth pattern, we propose a 3D model of a typical QD-Au HNC as shown in Figure 1g. The QD host, modeled as a quasi-spherical polyhedron, possesses five Au patches: three patches are located on three of the six "equatorial" $\{1\overline{2}10\}_{QD}$ facets (shown in light blue in Figure 1g), and two patches are located on $\{1\overline{2}15\}_{QD}$ facets (shown in green in Figure 1g), with one at the "top" and one at the "bottom" of the QD. This particular placement of Au patches maximizes their mutual distances on the QD surface, to account for effects of lattice strain and surface energy, in good agreement with previous reports.³⁵ While deviations from this idealized configuration of Au patches certainly occur in our HNC ensembles, we have confirmed the accuracy of our HNC model via 3D electron tomography measurements at a singleparticle level. Snapshots of a single HNC in the electron tomography movie at different orientations while rotating along the [1010] axis of WZ crystal match our HNC model well (Figure 1g,h and Movie S2).

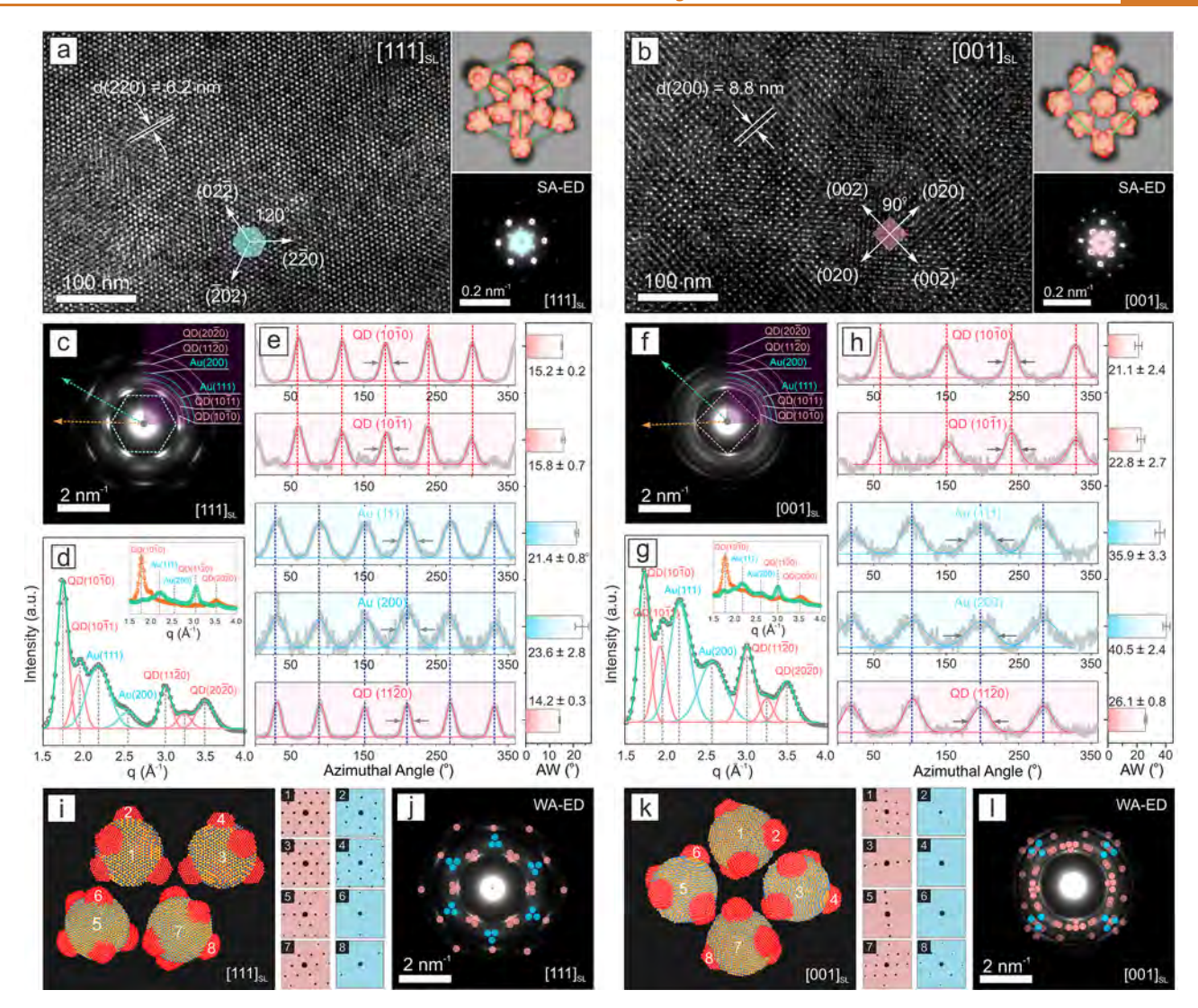


Figure 3. Dual atomic coherence in the QD-Au HNC SLs. (a, b) Representative TEM images of a HNC SL viewed along $[111]_{SL}$ (a) and $[001]_{SL}$ (b) SL projections. Insets: 3D HNC models of the fcc SL unit cell (top) and the SA-ED patterns of the TEM images (bottom). (c) WA-ED pattern along $[111]_{SL}$. (d) 2D integration of lattice peaks from the WA-ED pattern shown in (c). Inset: linear radial profiles, which are produced by the corresponding dotted lines in (c). (e) Azimuthal profiles of corresponding lattice peaks from the WA-ED pattern shown in (c). AW denotes the azimuthal width. (f) WA-ED pattern along $[001]_{SL}$. (g) 2D integration of lattice peaks from the WA-ED pattern shown in (f). Inset: linear radial profiles, which are produced by the corresponding dotted lines in (f). (h) Azimuthal profiles of the corresponding lattice peaks from the WA-ED pattern shown in (f). (i) Atomistic model of HNCs in the SL and FFT patterns showing dual atomic coherences. (j) Computer-simulated WA-ED pattern along $[111]_{SL}$. (k) Atomistic model and FFT patterns showing dual atomic coherences. (l) Computer-simulated WA-ED pattern along $[001]_{SL}$.

The appreciable size of Au patches (i.e., 4.2 nm in diameter on average) allowed us to conduct a detailed study of the epitaxial relationship between QD and Au constituents using high-resolution TEM (HR-TEM) (Figure 2). Six HR-TEM images of representative HNCs, viewed along two different crystallographic directions of the QD (i.e., [0001]_{OD} and [1111]_{OD}), are shown in Figure 2a-f. To infer the crystallographic relationship between QD host and Au patches, we compared the fast Fourier transformation (FFT) patterns of the lattice fringes determined in the QD and Au regions in the HR-TEM to simulated electron diffraction (ED) patterns of the atomistic HNC model we proposed. We first discuss the four QDs viewed along the [0001]_{OD} direction (Figure 2a-d). From this viewing direction, Au patches mainly appeared around the perimeter of the QD, consistent with their preferential growth on the $\{1\overline{2}10\}_{QD}$ "equatorial" QD facets

(Figure 1g,h). HR-TEM images clearly displayed lattice fringes of $\{10\overline{1}0\}_{QD}$, $\{1\overline{2}10\}_{QD}$, $\{111\}_{Au}$, and $\{002\}_{Au}$ (Figure 2a-d). FFT patterns obtained from Au patches (highlighted in orange) all showed a quasi-6-fold rotational symmetry (Figure 2a-d), consistent with simulated ED patterns along the [110]_{Au} direction of the face-centered cubic (fcc) crystal structure of gold. This observation suggests an epitaxial relationship of $[110]_{Au}//[0001]_{QD}$ (i.e., the $[110]_{Au}$ direction is parallel to the [0001]_{QD} direction; Figure 2a-d). This epitaxial relationship implies that Au patches grow on the $\{11\overline{2}0\}_{QD}$ QD facets through contacts of $\{111\}_{Au}$ and/or $\{002\}_{Au}$ crystal planes (i.e., $(\overline{1}11)_{Au}//(11\overline{2}0)$ and/or $(002)_{Au}/(11\overline{2}0)_{OD}$) (Figure S3). We note that, in a small number of cases (~3% of all the observed cases, ~100 HNCs analyzed), Au patches growing on the {1010}_{OD} facets were also observed; however, the same epitaxial relationship (i.e.,

 $(\overline{1}11)_{Au}//(11\overline{2}0)_{QD}$ and/or $(002)_{Au}//(11\overline{2}0)_{QD})$ was maintained in these cases (Figure S4).

An analogous HR-TEM analysis of HNCs viewed along the [1101]_{OD} direction confirmed the crystallographic relationship proposed above (Figure 2e,f). In this viewing direction, FFT patterns of the Au patches suggest that the $[010]_{Au}$ direction is approximately aligned with [1101]_{QD}. The epitaxial relationship of $\{002\}_{Au}/\{11\overline{2}0\}_{QD}$ was also suggested by analyzing these HR-TEM images and the corresponding FFT and simulated ED patterns (Figure 2e,f). Some additional HR-TEM images with similar crystal orientations are shown in Figure S5. Finally, we carried out HR-HAADF-STEM measurements to obtain a direct visualization of the lattice orientations at the interface between QD and Au crystal domains of a single HNC (Figure 2g-k). HR-HAADF-STEM images showed that the HNCs viewed along $[12\overline{1}3]_{QD}$ and $[01\overline{1}0]_{QD}$ directions and patterns of Cd and Au atoms are in good agreement with our proposed atomistic model. Notably, the epitaxial relationship of $[110]_{Au}/[0001]_{OD}$ (i.e., $(002)_{Au}//(1120)_{OD}$ and/or $(111)_{Au}//(1120)_{OD}$ is different from the typical relationship of $[110]_{fcc}//[1210]_{hcp}$ (i.e., $\{111\}_{fcc}//\{0001\}_{hcp}$) that has been commonly observed by others. S1-53 However, previous works usually involved hightemperature annealing processes to achieve such a typical epitaxial relationship. ⁵¹ In contrast, the epitaxial relationship observed in our case can be attributed to the limited domain size (<5 nm) of the Au patches and relatively low synthetic temperature (i.e., 80 °C). Another unconventional epitaxial relationship has also been reported in spherical CdS-Au systems under ambient conditions.5

Dual Atomic Lattice Coherence in Self-Assembled QD-Au HNC-SLs. The well-controlled number and geometrical configuration of Au patches on QD hosts, as well as their consistent epitaxial relationship, allowed us to produce HNC-SLs with orientational order and structural complexity. Upon solvent evaporation, HNCs assemble into an fcc SL, with a lattice parameter (a) of 17.6 nm, corresponding to an HNC center-to-center distance of 12.4 nm between the nearestneighbor HNCs (Figure 3a,b and Figure S6). In order to characterize HNC orientations within the SL, we performed small- and wide-angle ED (SA-/WA-ED) measurements along the $[111]_{SL}$ and $[001]_{SL}$ SL directions. The SA-ED patterns shown in the insets of Figure 3a,g confirmed the fcc structure with the assigned crystallographic projections (i.e., [111]_{SL} and [001]_{SL} projections). WA-ED patterns clearly showed defined and localized signals from both QD hosts and Au patches (Figure 3c-e,f-h and Figure S7), indicating a substantial degree of atomic coherence from both constituents.

To understand the detailed atomic lattice orientation relationship, we first discuss the WA-ED patterns of HNCs viewed along $[111]_{SL}$. The localized diffraction spots in WA-ED patterns obtained from the $[111]_{SL}$ projection can be assigned to $\{10\overline{1}0\}_{QD}$, $\{10\overline{1}1\}_{QD}$, $\{111\}_{Aw}$, $\{200\}_{Aw}$, $\{11\overline{2}0\}_{QD}$ and $\{20\overline{2}0\}_{QD}$ lattice planes, respectively, from the inside to the outside of diffraction rings shown in Figure 3c. The corresponding 2D integration of the WA-ED pattern is shown in Figure 3d. The fitted peaks and calculated d spacings are consistent with QD and Au lattice plane assignments (Figure 3d and Table S2). Similar to our previous study, ³⁵ WA-ED signals that originate from $\{10\overline{1}0\}_{QD}$ and $\{11\overline{2}0\}_{QD}$ WZ lattice planes are produced by QD hosts whose $[0001]_{QD}$ orientation is aligned with $[111]_{SL}$, while signals originating from $\{10\overline{1}1\}_{QD}$ planes are produced by QD hosts whose $[21\overline{13}]_{QD}$

orientation is aligned with [111]_{SL} (Figure 3c and Figure S7). These assignments were further supported by HR-TEM images of a {111}_{SL} surface (Figure S8), where QD hosts with both $[0001]_{QD}$ and $[2\overline{113}]_{QD}$ alignment can be unambiguously identified. The population of QDs with [0001]_{OD} alignment is noticeably larger than that of QDs with [2113]_{OD} orientation, as evidenced by the approximately 2-fold larger signal intensity originating from $\{1010\}_{QD}$ planes as compared to {1011}_{QD} planes (Figure 3c,d). In addition to QD hosts, Au patches also show a significant degree of atomic lattice alignment. WA-ED signals originating from {111}_{Au} and {200}_{Au} lattice planes were observed as localized signals with a 6-fold symmetry (Figure 3c), as opposed to featureless diffraction rings. The relationship between atomic plane alignments of both QD and Au can be inferred from the azimuthal profile of WA-ED patterns. As shown in Figure 3e, the azimuthal profiles of ED patterns from $\{10\overline{10}\}_{OD}$ and {1011}_{OD} lattice planes are out-of-phase with patterns from $\{111\}_{Au}$ and $\{200\}_{Au}$ planes. In contrast, the azimuthal profile of the {1120}_{QD} diffraction pattern is in-phase with the $\{111\}_{Au}$ and $\{200\}_{Au}$ profiles (Figure 3e). This result is consistent with the epitaxial relationship between QD host and Au_patches (i.e., $(\overline{1}11)_{Au}//(11\overline{20})_{QD}$ and/or $(002)_{Au}//$ (1120)_{QD}) and the proposed HNC model discussed above (Figures 1 and 2).

We performed an analogous analysis of the WA-ED patterns obtained in [001]_{SL} projection of the HNC-SL (Figure 3f-h). Patterns with 4-fold rotational symmetry were observed, including with localized diffraction signals for $\{10\overline{1}0\}_{QD}$, $\{1011\}_{QD}$, $\{111\}_{Aw}$ $\{200\}_{Aw}$ $\{1120\}_{QD}$, and $\{2020\}_{QD}$ atomic planes (Figure 3f), as assigned from fitting to the integrated WA-ED pattern (Figure 3g and Table S2). Importantly, the azimuthal plots obtained from the [001]_{SL} WA-ED pattern showed the same phase behavior across QD and Au lattice planes as observed in the [111]_{SL} projection (Figure 3h,g), providing further evidence for the atomic coherence of both QD and Au lattices. It is worth noting that epitaxy between thin films has been well developed and can be characterized by various techniques, including high-resolution XRD with coupled scan, grazing incidence XRD, and pole figure. 55-57 Characterizations of interfacial epitaxy of multicomponent nanoparticles often rely only on imaging of individual particles using HR-TEM with limited statistics. The analysis demonstrated here shows that resolving orientational alignments from self-assemblies of HNCs with the help of WA-ED can be a powerful strategy to determine nanointerfacial epitaxy from ensemble measurements with statistical significance.

The degree of orientational order of NC-SLs can be gauged by the azimuthal widths of localized WA-ED signals.⁵⁸ In our case, the substantial widths of some of the WA-ED patterns suggest that the orientational order of HNCs in the SLs can deviate from the idealized scenario discussed above. To quantify these differences, we plot azimuthal profiles of each diffracted peak shown in the WA-ED patterns (Figure 3d,g). Along the [111]_{SL} projection, the azimuthal widths (full-width at half-maximum, fwhm of each azimuthal peak) were $\sim 15^{\circ}$ for all three QD lattice planes and $\sim 23^{\circ}$ for Au (Figure 3e). The WA-ED pattern acquired from the [001]_{SL} projection are noticeably broader (Figure 3h). In both cases, the azimuthal widths are clearly larger than the reported values (~10°) for Pb-chalcogenide NC-SLs (Table S3),⁵⁹ which we attribute to two reasons: variations in HNC building blocks (i.e., number, size, epitaxy, and geometrical position of Au patches on QD

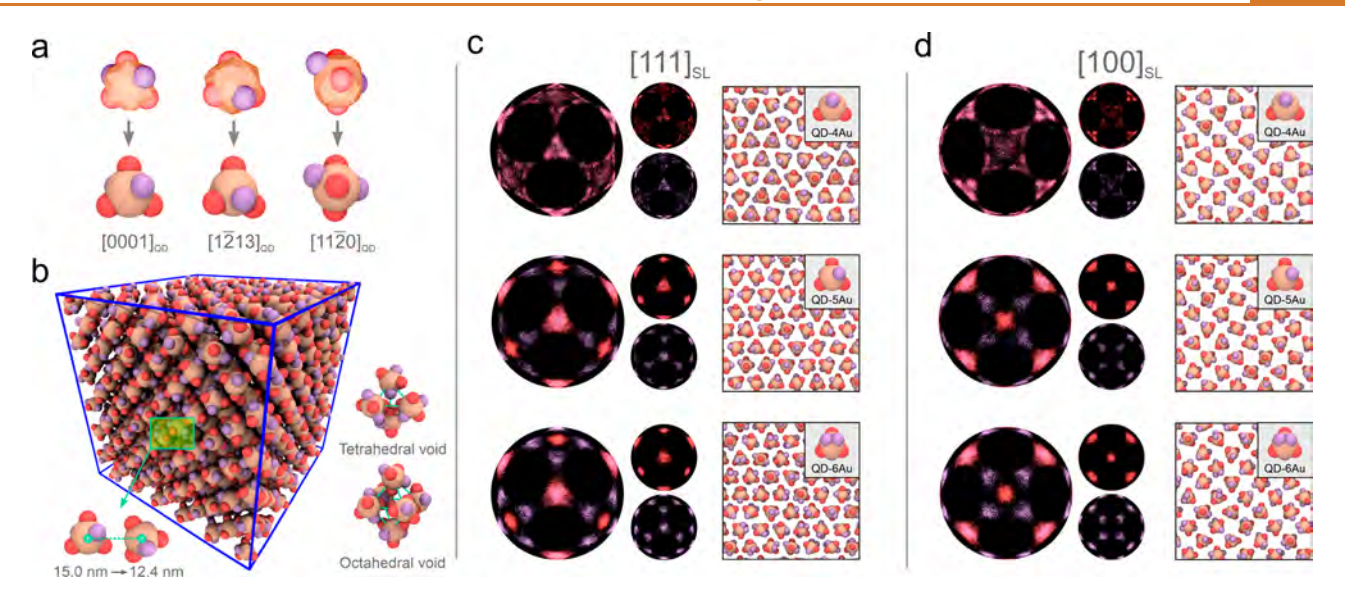


Figure 4. MD simulations of fcc HNC-SLs assembled from the QD-Au HNCs with four, five, and six Au patches. (a) Comparison of QD-5Au (five Au patches per QD host) polyhedral HNC model (top) and the corresponding spherical QD-Au HNC model used in simulations (bottom), viewed along different lattice WZ directions of QD. (b) Snapshot of a simulation box showing an fcc SL of QD-5Au HNCs. Also shown are excerpts from the same snapshot, highlighting the tetrahedral and octahedral voids in the HNC-SL. (c, d) Orientational order diagrams (left) of fcc SL of HNCs with four (top), five (middle), and six (bottom) Au patches, viewed along $[111]_{SL}$ (c) and $[100]_{SL}$ (d) SL projections. Snapshots (right) show $(111)_{SL}$ and $(100)_{SL}$ monolayers of HNC in the SL. Patches on $\{1215\}_{QD}$ facets are shown in purple and patches on equatorial $\{1110\}_{QD}$ facets in red.

host) and the symmetry mismatch between hexagonal WZ-QD hosts and the assembled fcc SL (Figure S9).³⁵

To understand the origin of the ED signals, we analyze an idealized atomistic model of four HNCs viewed along the [111]_{SL} projection (Figure 3i), where QDs preferably adopt $[0001]_{OD}$ (top two HNCs) and $[2\overline{11}3]_{OD}$ (bottom two HNCs) orientations. Due to the epitaxy between QD and Au, (partial) coherence of Au lattices is achieved (Figure 3i). We then simulated the collective WA-ED pattern resulting from all possible QD and Au orientations that should present in the $[111]_{SL}$ projection (Figure S10 and Tables S4 and S5). The simulated pattern shows decent agreement with the experimental WA-ED pattern (Figure 3j and Figure S11). The same kind of analysis was conducted for the ED results from the [001]_{SL} projection (Figure 3k,l). Signals that originate from $\{10\overline{1}0\}_{QD}$, $\{10\overline{1}1\}_{QD}$, and $\{11\overline{2}0\}_{QD}$ WZ lattice planes are produced from the QDs with $[01\overline{1}1]_{QD}$ and $[\overline{2}113]_{QD}$ orientations, which are connected to [2113]_{OD}-oriented QDs in the $[111]_{SL}$ projection via appropriate rotations (Figure 3k, Figure S12, and Table S6). Signals that originate from $\{111\}_{Au}$ and $\{200\}_{Au}$ of Au patch crystals can also be reproduced via the same series of rotations of HNC building blocks (Figure 3k and Table S7). The simulated ED pattern (generated based on all possible HNC orientations (Tables S6 and S7)) also shows a comparable level of agreement with the experimentally obtained pattern along the [001]_{SL} projection (Figure 31 and Figure S13). Moreover, the ED simulation results show that the broad diffraction patterns observed in the [001]_{SL} projection are at least partially induced by the symmetry mismatch between the hexagonal WZ-QD and the assembled cubic fcc SL: the simulated ED pattern of the idealized HNC assembly in the [001]_{SL} projection shows diffraction signals more dispersed than those obtained in the [111]_{SL} direction (Figure 3j,l). Additionally, as we showed previously, the atomic lattice coherence of QD hosts in the SL is a direct result of the interactions of Au patches on otherwise

near-spherical QD hosts.³⁵ Modest variations in the size, number, and location of Au patches limit the degree of orientational order than can be achieved in the final SL.

MD Simulations of the QD-Au HNC-SLs Formation. To probe the microscopic origins of the orientational order observed in our HNC-SL, we simulated the dynamics of model HNCs in an fcc SL. HNCs are modeled as spherical particles with 8.0 nm diameter (representing QD hosts), rigidly connected with four, five, or six smaller spherical particles (4.2 nm diameter, representing Au patches). Au patches are placed on the surface of the QD host in positions corresponding to the centers of imaginary {1215}_{QD} and {1110}_{OD} facets of an underlying WZ lattice. The resulting HNCs with five Au patches are illustrated in Figure 4a (Figure S14). Note that this specific placement of Au patches maximizes the smallest distance between any pair of patches on the HNC. Interactions between HNCs were adopted from a recent work³⁵ and implicitly account for dense monolayers of ligands bound to both QD and Au surfaces and van der Waals (vdW) interactions between Au patches (Figure S14 and Table S8).

We first confirmed that our model HNCs indeed self-assemble into close-packed superlattices. When initiated from dispersed configurations and subjected to modest pressure, a periodically replicated system of 864 HNCs formed an fcc superlattice with several grain boundaries (Movie S3). Such defects are typical for MD simulations of self-assembly, which can only access time scales that are much shorter than experimental time scales. To carefully assess the orientational order of HNCs, we then performed an MD simulation of 864 HNCs prearranged on a defect-free fcc lattice. To equilibrate the rotational degrees of freedom of HNC in the superlattice, we initially increase the effective thickness of the ligand shell that covers the QDs (via the interaction parameter Δ , see Methods in the Supporting Information), resulting in a nearest-neighbor distance of 15 nm (significantly larger than

the experimentally measured distance of 12.4 nm). Under these conditions, Au patches on neighboring HNCs do not interact strongly and HNCs can freely rotate (Movie S4). Then, we slowly decrease the thickness of the ligand shell until the experimental nearest-neighbor distance of 12.4 nm is reached (Figure 4b and Movie S4). This simulated SL contraction mimics the final stages of a self-assembly experiment using solvent evaporation. Even before the final lattice constant is reached, HNCs settle into well-defined orientations and remain there for the remainder of the simulation, except for small vibrations (Figure 4b and Movie S4).

To characterize the orientations of HNCs in the SL, we plot orientational order diagrams (OOD) along both the [111]_{SL} and [001]_{SL} SL projections, as illustrated in Figure 4c,d. Blue and red dots in these diagrams indicate the positions of Au patches on $\{1\overline{2}15\}_{QD}$ and $\{1\overline{2}10\}_{QD}$ facets, respectively, of all HNCs at a given moment in time during the MD simulation (Figure 4c,d). These diagrams therefore provide a map of all possible positions of Au patches and, therefore, HNC orientations. As is evident from OODs in Figure 4c,d, HNCs with four, five, and six Au patches show qualitatively similar behavior: Au patches are located in regions corresponding to the six octahedral voids (located in equivalent [100]_{SI} directions) and eight tetrahedral voids (in equivalent [111]_{SL} directions) that surround a given HNC in the fcc SL (Figure 4b-d). HNCs with only four patches have near-perfect tetrahedral symmetry, and a large number of different orientations can be realized (Figure 4c,d, top panels). In HNCs with five Au patches, however, this symmetry is broken and HNC orientations are further confined. In this case, Au patches on $\{1\overline{2}10\}_{QD}$ facets (represented in red in Figure 4c,d, middle panels) are pointing in the [100]_{SL} and [111]_{SL} directions (away from the HNC center), with typical angular deviations smaller than 10°. Based on the HNC orientations observed in our simulations, we have generated the corresponding ED diffraction patterns in the [111]_{SL} projection, which reproduce prominent features of our experimental diffraction patterns (Figure S15). Interestingly, adding a sixth patch does not change the OOD significantly (Figure 4c,d, bottom panels), suggesting that the orientational order observed in our experiments is robust with respect to small variations in the number of Au patches.

Two driving forces favor the aggregation of Au patches in the voids of the *fcc* SL: vdW forces between Au patches and effects of volume exclusion, which disfavor the aggregation of large Au patches in the limited space between nearest-neighbor HNCs. Our simulations suggest that volume exclusion of Au patches alone is sufficient to produce the observed HNC orientational patterns. MD simulations with purely repulsive interactions between Au patches result in essentially the same OODs (Figure S16). Our simulations therefore suggest that the number, size, and placement of Au patches are critical parameters that, when controlled synthetically to high precision, can give rise to different types of structural order and atomic lattice coherence in NC-SLs.

CONCLUSION

In conclusion, our study describes a strategy to control the orientational order of self-assembled colloidal hybrid HNCs, achieving SLs with an atomic lattice coherence of both HNC constituents. Uniform QD-Au HNCs were synthesized first with a consistent placement of Au patches and an epitaxial

relationship between the two components. These HNCs, once assembled, can concurrently achieve atomic alignments for both the QD host and Au patches, due to the epitaxial relationship between the two components of individual HNCs. In addition, due to the high crystallinity of the relatively large Au patches (~4.2 nm), we demonstrated a procedure to analyze electron diffraction patterns of HNC-SLs, providing detailed orientations of the HNCs inside superlattices and confirming the epitaxial relationship between QD and Au within individual HNCs as well as the HNC-SLs with statistical significance. MD simulations indicate that the observed dual atomic coherence is linked to the number, size and placement of gold patches. Our study reveals the possibility of controlling the orientational orders and atomic lattice coherence of assemblies beyond single-component colloidal systems. The synthesis of epitaxially defined QD-Au HNCs and the detailed analytical method for characterizations of the nanointerfacial epitaxy between the two components (commonly studied for bulk/thin film materials) can be of importance to related research fields beyond nanoscale materials. Our strategy of controlling and understanding multicomponent orientational orders of self-assembled colloidal particles can likely be extended to other hybrid and heterostructure nanoconstructs. We anticipate that, with further synthetic advancements of complex hybrid nanomaterials with rigid epitaxial relations across multicomponents, creating advanced functional materials with synergistic chemical and physical properties aroused from multiatomistic lattice coherences becomes feasible.

METHODS

Synthesis of CdSe-CdS Core—Shell Quantum Dots (QDs). CdSe-CdS core—shell QDs were synthesized using a previously published method with minor modification. ⁶¹

Synthesis of CdSe Core. Briefly, 60 mg of CdO, 280 mg of ODPA and 3.0 g of TOPO were placed in a 50 mL flask. The mixture was heated to 150 °C and degassed under vacuum for 1 h. Under a nitrogen flow, the reaction mixture was further heated to 320 °C to form a colorless clear solution. After adding 2.0 mL of TOP to the solution, the temperature was quickly increased to 380 °C, at which point a Se/TOP (60 mg of Se in 0.5 mL of TOP) solution was injected quickly into the flask. When the CdSe core QDs reached the desired size, the reaction was terminated by removing the heat. After cooling to room temperature, the resulting CdSe QDs were precipitated by adding acetone and redispersed in hexane for further use.

CdS Shell Growth. A hexane solution containing 200 nmol of CdSe core QDs was loaded in a mixture of 4.0 mL of ODE and 4.0 mL of OAm. The reaction solution was degassed under vacuum at room temperature for 1 h and at 120 °C for another 20 min to completely remove the hexane, water, and oxygen inside the reaction solution. After that, the reaction solution was heated to 240 °C, at which point a desired amount of cadmium(II) oleate (six monolayers (MLs), diluted in 4.0 mL of ODE) and 1.2 equiv of ODT (diluted in 4.0 mL of ODE) were injected into the growth solution at a rate of 2 ML/h using a syringe pump. Meanwhile, the reaction temperature was further raised to 310 °C and maintained there for the rest of the reaction. During the growth, 1.0 mL of oleic acid was injected every 1 h. After the precursor infusion was finished, another 1.0 mL of oleic acid was quickly injected and the solution was further annealed at 310 °C for 30 min. The resulting CdSe-CdS core-shell QDs were precipitated by adding acetone and then redispersed in toluene as a stock solution.

Synthesis of QD-Au Heterostructural Nanocrystals (HNCs). QD-Au host-satellite HNCs were synthesized using a modified method similar to that in our previous report. 35,62 Typically, 5.0 mg of as-synthesized CdSe-CdS core—shell QDs was dispersed in 10 mL of

ODE with stirring. A gold precursor stock solution was prepared by adding 30 mg of AuCl₃, 154 mg of DTAB, and 0.5 mL of OAm to 7.0 mL of toluene and sonicating the mixture for 15 min. The solution eventually turned light yellow. A 4.0 mL portion of the gold precursor was first filtered using 25 mm syringe filter with a 0.2 μ m PTFE membrane and was then mixed with 20.0 mL of ODE. The QD solution was then gradually heated to 80 °C, and gold precursors were injected into the QD solution at a rate of 2 mL/min. The reaction mixture was maintained at 80 °C for 1 h. The resulting QD-Au HNCs were precipitated by adding a mixture of ethanol and methanol and then redispersed in toluene. After the Au satellite growth, the emission of the QD is totally quenched.

Formation of HNC-Superlattices (SLs). The resulting QD-Au HNCs were dispersed in toluene and diluted to \sim 2.0 mg/mL. A TEM grid was first placed on a clean silicon substrate, and then \sim 50 μ L of the toluene solution was dropped on the TEM grid. The sample was further covered with a glass Petri dish to ensure a slow solvent evaporation.

Molecular Dynamics (MD) Simulations. Parameters for Au–Au, QD–QD, and Au–QD interactions were adapted from previous work.³⁵ All interactions are modeled with an "expanded" Lennard–Jones potential as implemented in LAMMPS:

$$u(r) = 4\varepsilon \left[\left(\frac{\sigma}{r - \Delta} \right)^{12} - \left(\frac{\sigma}{r - \Delta} \right)^{6} \right]$$
 (1)

All interaction potentials were cut and shifted to zero at a distance of Δ + r_{cut} . Interaction parameters are provided in Table S8.

Interactions described by the above potentials implicitly take the presence of ligands on QD and Au particles into account, as illustrated in Figure S14. For QD/QD interactions, the value of $\varepsilon=6.0$ kcal/mol describes substantial cohesive interactions between ligand shells on QDs. The results of our simulations are insensitive to this value, as long as the cohesive energy of QDs is large enough to stabilize the fcc superlattice. The parameter $\Delta_{\rm QD}$ determines the effective thickness of the ligand shell. In our simulations, we vary $\Delta_{\rm QD}$ between 142 and 92 Å. At large values, HNCs can freely rotate; as $\Delta_{\rm QD}$ is decreased, HNCs settle into well-defined orientations, as described in the main text. Attractive interactions between Au nanocrystals ($\varepsilon=1.5$ kcal/mol) represent van der Waals interactions between Au cores across a medium of hydrocarbon ligands. Interactions between QD and Au particles are purely repulsive, which is achieved by cutting the potential at its minimum and shifting it to zero.

ASSOCIATED CONTENT

Supporting Information

The Supporting Information is available free of charge at https://pubs.acs.org/doi/10.1021/acsnano.2c06167.

Experimental and simulation methods, additional figures, and additional characterization of QD-Au HNCs and the corresponding SLs (PDF)

Movie S1 3D electron tomography movie of large-area dispersed QD-Au HNCs (AVI)

Movie S2 3D electron tomography movie of a single QD-Au HNC (AVI)

Movie S3 MD simulation of 864 QD-Au HNCs self-assembling into an fcc SL (AVI)

Movie S4 MD simulation of an fcc SL of QD-Au HNCs. During the thickness of the ligand shell is coninuously decreased and HNCs settle into well-defined orientations (AVI)

AUTHOR INFORMATION

Corresponding Authors

Ou Chen – Department of Chemistry, Brown University, Providence, Rhode Island 02912, United States;

orcid.org/0000-0003-0551-090X; Email: ouchen@brown.edu

Michael Grünwald — Department of Chemistry, University of Utah, Salt Lake City, Utah 84112, United States; Email: michael.gruenwald@utah.edu

Authors

Hua Zhu — Department of Chemistry, Brown University, Providence, Rhode Island 02912, United States;
ocid.org/0000-0003-2733-7837

Zhaochuan Fan — Department of Chemistry, University of Utah, Salt Lake City, Utah 84112, United States;
orcid.org/0000-0001-9492-5722

Siyuan Song — School of Engineering, Brown University, Providence, Rhode Island 02912, United States

Dennis Eggert — Department of Otorhinolaryngology, University Medical Center Hamburg-Eppendorf, Hamburg 20246, Germany; Heinrich Pette Institute-Leibniz Institute for Experimental Virology, Hamburg 20251, Germany

Yuzi Liu — Center for Nanoscale Materials, Argonne National Laboratory, Argonne, Illinois 60439, United States;
orcid.org/0000-0002-8733-1683

Wenwu Shi – Department of Chemistry, Brown University, Providence, Rhode Island 02912, United States

Yucheng Yuan – Department of Chemistry, Brown University, Providence, Rhode Island 02912, United States

Kyung-Suk Kim — School of Engineering, Brown University, Providence, Rhode Island 02912, United States

Complete contact information is available at: https://pubs.acs.org/10.1021/acsnano.2c06167

Author Contributions

All authors have given approval to the final version of the manuscript.

Funding

O.C. acknowledges support from the National Science Foundation under Award Nos. DMR-1943930 and CMMI-1934314. O.C. also acknowledges support from the Camille & Henry Dreyfus Foundation through the Camille Dreyfus Teacher-Scholar Award Program, the Alfred P. Sloan Foundation through Sloan Research Fellowship Award program, and the 3M Foundation through the Non-Tenured Faculty Award program. Z.F. and M.G. acknowledge support by the National Science Foundation under Grant No. DMR-1848499. This work was performed, in part, at the Center for Nanoscale Materials, a U.S. Department of Energy Office of Science User Facility, supported by the U.S. DOE, Office of Basic Energy Sciences, under Contract No. DE-AC02-06CH11357.

Notes

The authors declare no competing financial interest.

ACKNOWLEDGMENTS

TEM, XRD, and XPS measurements were performed at the Electron Microscopy Facility and NanoTools Facility in the Institute for Molecular and Nanoscale Innovation (IMNI) at Brown University. The support and resources of the Center for High Performance Computing at the University of Utah are gratefully acknowledged.

REFERENCES

- (1) Murray, C. B.; Kagan, C. R.; Bawendi, M. G. Self-Organization of CdSe Nanocrystallites into 3-Dimensional Quantum-Dot Superlattices. *Science* **1995**, 270 (5240), 1335–1338.
- (2) Boles, M. A.; Engel, M.; Talapin, D. V. Self-Assembly of Colloidal Nanocrystals: From Intricate Structures to Functional Materials. *Chem. Rev.* **2016**, *116* (18), 11220–11289.
- (3) Bishop, K. J. M.; Wilmer, C. E.; Soh, S.; Grzybowski, B. A. Nanoscale Forces and Their Uses in Self-Assembly. *Small* **2009**, 5 (14), 1600–1630.
- (4) Pileni, M. P. Self-Assembly of Inorganic Nanocrystals: Fabrication and Collective Intrinsic Properties. *Acc. Chem. Res.* **2007**, *40* (8), 685–693.
- (5) Tan, R.; Zhu, H.; Cao, C.; Chen, O. Multi-Component Superstructures Self-Assembled from Nanocrystal Building Blocks. *Nanoscale* **2016**, *8* (19), 9944–9961.
- (6) Deng, K. R.; Luo, Z. S.; Tan, L.; Quan, Z. W. Self-Assembly of Anisotropic Nanoparticles into Functional Superstructures. *Chem. Soc. Rev.* **2020**, *49* (16), 6002–6038.
- (7) Dijkstra, M.; Luijten, E. From Predictive Modelling to Machine Learning and Reverse Engineering of Colloidal Self-Assembly. *Nat. Mater.* **2021**, 20 (6), 762–773.
- (8) Nie, Z. H.; Petukhova, A.; Kumacheva, E. Properties and Emerging Applications of Self-Assembled Structures Made from Inorganic Nanoparticles. *Nat. Nanotechnol.* **2010**, *5* (1), 15–25.
- (9) Nykypanchuk, D.; Maye, M. M.; van der Lelie, D.; Gang, O. DNA-Guided Crystallization of Colloidal Nanoparticles. *Nature* **2008**, 451 (7178), 549–552.
- (10) Lin, H. X.; Lee, S. M.; Sun, L.; Spellings, M.; Engel, M.; Glotzer, S. C.; Mirkin, C. A. Clathrate Colloidal Crystals. *Science* **2017**, 355 (6328), 931–935.
- (11) Nagaoka, Y.; Zhu, H.; Eggert, D.; Chen, O. Single-Component Quasicrystalline Nanocrystal Superlattices through Flexible Polygon Tiling Rule. *Science* **2018**, 362 (6421), 1396–1400.
- (12) Nagaoka, Y.; Tan, R.; Li, R.; Zhu, H.; Eggert, D.; Wu, Y. A.; Liu, Y.; Wang, Z.; Chen, O. Superstructures Generated from Truncated Tetrahedral Quantum Dots. *Nature* **2018**, *561* (7723), 378–382.
- (13) Wang, S. Z.; Lee, S. M.; Du, J. S.; Partridge, B. E.; Cheng, H. F.; Zhou, W. J.; Dravid, V. P.; Lee, B.; Glotzer, S. C.; Mirkin, C. A. The Emergence of Valency in Colloidal Crystals through Electron Equivalents. *Nat. Mater.* **2022**, *21*, 580–587.
- (14) Wang, T.; Zhuang, J.; Lynch, J.; Chen, O.; Wang, Z.; Wang, X.; LaMontagne, D.; Wu, H.; Wang, Z.; Cao, Y. C. Self-Assembled Colloidal Superparticles from Nanorods. *Science* **2012**, 338 (6105), 358–363.
- (15) Tang, Z. Y.; Kotov, N. A.; Giersig, M. Spontaneous Organization of Single Cdte Nanoparticles into Luminescent Nanowires. *Science* **2002**, *297* (5579), 237–240.
- (16) Wu, L.; Willis, J. J.; McKay, I. S.; Diroll, B. T.; Qin, J.; Cargnello, M.; Tassone, C. J. High-Temperature Crystallization of Nanocrystals into Three-Dimensional Superlattices. *Nature* **2017**, *548* (7666), 197–201.
- (17) Tang, L. Q.; Vo, T.; Fan, X. X.; Vecchio, D.; Ma, T.; Lu, J.; Hou, H.; Glotzer, S. C.; Kotov, N. A. Self-Assembly Mechanism of Complex Corrugated Particles. *J. Am. Chem. Soc.* **2021**, *143* (47), 19655–19667.
- (18) Zhang, J. Y.; Santos, P. J.; Gabrys, P. A.; Lee, S.; Liu, C.; Macfarlane, R. J. Self-Assembling Nanocomposite Tectons. *J. Am. Chem. Soc.* **2016**, *138* (50), 16228–16231.
- (19) Yi, C. L.; Zhang, S. Y.; Webb, K. T.; Nie, Z. H. Anisotropic Self-Assembly of Hairy Inorganic Nanoparticles. *Acc. Chem. Res.* **2017**, *50* (1), 12–21.
- (20) Ye, X.; Chen, J.; Eric Irrgang, M.; Engel, M.; Dong, A.; Glotzer, S. C.; Murray, C. B. Quasicrystalline Nanocrystal Superlattice with Partial Matching Rules. *Nat. Mater.* **2017**, *16* (2), 214–219.
- (21) Quan, Z. W.; Xu, H. W.; Wang, C. Y.; Wen, X. D.; Wang, Y. X.; Zhu, J. L.; Li, R. P.; Sheehan, C. J.; Wang, Z. W.; Smilgies, D. M.; Luo,

- Z. P.; Fang, J. Y. Solvent-Mediated Self-Assembly of Nanocube Superlattices. J. Am. Chem. Soc. 2014, 136 (4), 1352–1359.
- (22) Smith, D. K.; Goodfellow, B.; Smilgies, D. M.; Korgel, B. A. Self-Assembled Simple Hexagonal AB(2) Binary Nanocrystal Superlattices: Sem, Gisaxs, and Defects. *J. Am. Chem. Soc.* **2009**, *131* (9), 3281–3290.
- (23) Kostiainen, M. A.; Hiekkataipale, P.; Laiho, A.; Lemieux, V.; Seitsonen, J.; Ruokolainen, J.; Ceci, P. Electrostatic Assembly of Binary Nanoparticle Superlattices Using Protein Cages. *Nat. Nanotechnol.* **2013**, 8 (1), 52–56.
- (24) Kalsin, A. M.; Fialkowski, M.; Paszewski, M.; Smoukov, S. K.; Bishop, K. J.; Grzybowski, B. A. Electrostatic Self-Assembly of Binary Nanoparticle Crystals with a Diamond-Like Lattice. *Science* **2006**, 312 (5772), 420–424.
- (25) Wang, Y.; Chen, J.; Zhu, C. H.; Zhu, B. X.; Jeong, S. J.; Yi, Y.; Liu, Y.; Fiadorwu, J.; He, P.; Ye, X. C. Kinetically Controlled Self-Assembly of Binary Polymer-Grafted Nanocrystals into Ordered Superstructures Via Solvent Vapor Annealing. *Nano Lett.* **2021**, *21* (12), 5053–5059.
- (26) Coropceanu, I.; Janke, E. M.; Portner, J.; Haubold, D.; Nguyen, T. D.; Das, A.; Tanner, C. P. N.; Utterback, J. K.; Teitelbaum, S. W.; Hudson, M. H.; Sarma, N. A.; Hinkle, A. M.; Tassone, C. J.; Eychmüller, A.; Limmer, D. T.; Cruz, M. O. d. l.; Ginsberg, N. S.; Talapin, D. V. Self-Assembly of Nanocrystals into Strongly Electronically Coupled All-Inorganic Supercrystals. *Science* **2022**, *375* (6587), 1422–1426.
- (27) Wang, D.; Dasgupta, T.; van der Wee, E. B.; Zanaga, D.; Altantzis, T.; Wu, Y. T.; Coli, G. M.; Murray, C. B.; Bals, S.; Dijkstra, M.; van Blaaderen, A. Binary Icosahedral Clusters of Hard Spheres in Spherical Confinement. *Nat. Phys.* **2021**, *17* (1), 128.
- (28) Sun, Y. G. Interfaced Heterogeneous Nanodimers. *Natl. Sci. Rev.* 2015, 2 (3), 329–348.
- (29) Weidman, M. C.; Smilgies, D. M.; Tisdale, W. A. Kinetics of the Self-Assembly of Nanocrystal Superlattices Measured by Real-Time in Situ X-Ray Scattering. *Nat. Mater.* **2016**, *15* (7), 775–781.
- (30) Boneschanscher, M. P.; Evers, W. H.; Geuchies, J. J.; Altantzis, T.; Goris, B.; Rabouw, F. T.; van Rossum, S. A. P.; van der Zant, H. S. J.; Siebbeles, L. D. A.; Van Tendeloo, G.; Swart, I.; Hilhorst, J.; Petukhov, A. V.; Bals, S.; Vanmaekelbergh, D. Long-Range Orientation and Atomic Attachment of Nanocrystals in 2DHoneycomb Superlattices. *Science* 2014, 344 (6190), 1377–1380.
- (31) Cherniukh, I.; Rainò, G.; Stöferle, T.; Burian, M.; Travesset, A.; Naumenko, D.; Amenitsch, H.; Erni, R.; Mahrt, R. F.; Bodnarchuk, M. I.; Kovalenko, M. V. Perovskite-Type Superlattices from Lead Halide Perovskite Nanocubes. *Nature* **2021**, *593* (7860), 535–542.
- (32) Yi, C. L.; Liu, H.; Zhang, S. Y.; Yang, Y. Q.; Zhang, Y.; Lu, Z. Y.; Kumacheva, E.; Nie, Z. H. Self-Limiting Directional Nanoparticle Bonding Governed by Reaction Stoichiometry. *Science* **2020**, *369* (6509), 1369–1374.
- (33) Miszta, K.; de Graaf, J.; Bertoni, G.; Dorfs, D.; Brescia, R.; Marras, S.; Ceseracciu, L.; Cingolani, R.; van Roij, R.; Dijkstra, M.; Manna, L. Hierarchical Self-Assembly of Suspended Branched Colloidal Nanocrystals into Superlattice Structures. *Nat. Mater.* **2011**, *10* (11), 872–876.
- (34) Luo, B. B.; Kim, A.; Smith, J. W.; Ou, Z. H.; Wu, Z. X.; Kim, J.; Chen, Q. Hierarchical Self-Assembly of 3D Lattices from Polydisperse Anisometric Colloids. *Nat. Commun.* **2019**, *10*, 1815.
- (35) Zhu, H.; Fan, Z. C.; Yu, L.; Wilson, M. A.; Nagaoka, Y.; Eggert, D.; Cao, C.; Liu, Y. Z.; Wei, Z. C.; Wang, X. D.; He, J.; Zhao, J.; Li, R. P.; Wang, Z. W.; Grunwald, M.; Chen, O. Controlling Nanoparticle Orientations in the Self-Assembly of Patchy Quantum Dot-Gold Heterostructural Nanocrystals. *J. Am. Chem. Soc.* **2019**, *141* (14), 6013–6021.
- (36) Zhu, H.; Fan, Z.; Yuan, Y.; Wilson, M. A.; Hills-Kimball, K.; Wei, Z.; He, J.; Li, R.; Grunwald, M.; Chen, O. Self-Assembly of Quantum Dot-Gold Heterodimer Nanocrystals with Orientational Order. *Nano Lett.* **2018**, *18* (8), 5049–5056.
- (37) Udayabhaskararao, T.; Altantzis, T.; Houben, L.; Coronado-Puchau, M.; Langer, J.; Popovitz-Biro, R.; Liz-Marzán, L. M.; Vuković,

- L.; Král, P.; Bals, S.; Klajn, R. Tunable Porous Nanoallotropes Prepared by Post-Assembly Etching of Binary Nanoparticle Superlattices. *Science* **2017**, *358* (6362), 514–518.
- (38) Peng, L. T.; Ma, X. D.; Zhu, H.; Chen, O.; Wang, W. Influence of Local Structures on the Energy Transfer Efficiencies of Quantum-Dot Films. *Phys. Rev. B* **2020**, *102* (3), 035437.
- (39) Montanarella, F.; Urbonas, D.; Chadwick, L.; Moerman, P. G.; Baesjou, P. J.; Mahrt, R. F.; van Blaaderen, A.; Stoferle, T.; Vanmaekelbergh, D. Lasing Supraparticles Self-Assembled from Nanocrystals. *ACS Nano* **2018**, *12* (12), 12788–12794.
- (40) Cherniukh, I.; Sekh, T. V.; Rainò, G.; Ashton, O. J.; Burian, M.; Travesset, A.; Athanasiou, M.; Manoli, A.; John, R. A.; Svyrydenko, M.; Morad, V.; Shynkarenko, Y.; Montanarella, F.; Naumenko, D.; Amenitsch, H.; Itskos, G.; Mahrt, R. F.; Stöferle, T.; Erni, R.; Kovalenko, M. V.; Bodnarchuk, M. I. Structural Diversity in Multicomponent Nanocrystal Superlattices Comprising Lead Halide Perovskite Nanocubes. ACS Nano 2022, 16 (5), 7210–7232.
- (41) Kalesaki, E.; Delerue, C.; Smith, C. M.; Beugeling, W.; Allan, G.; Vanmaekelbergh, D. Dirac Cones, Topological Edge States, and Nontrivial Flat Bands in Two-Dimensional Semiconductors with a Honeycomb Nanogeometry. *Phys. Rev. X* **2014**, *4* (1), 011010.
- (42) Whitham, K.; Yang, J.; Savitzky, B. H.; Kourkoutis, L. F.; Wise, F.; Hanrath, T. Charge Transport and Localization in Atomically Coherent Quantum Dot Solids. *Nat. Mater.* **2016**, *15* (5), 557–563.
- (43) Kalesaki, E.; Evers, W. H.; Allan, G.; Vanmaekelbergh, D.; Delerue, C. Electronic Structure of Atomically Coherent Square Semiconductor Superlattices with Dimensionality Below Two. *Phys. Rev. B* **2013**, *88* (11), 115431.
- (44) Lazarenkova, O. L.; Balandin, A. A. Miniband Formation in a Quantum Dot Crystal. *J. Appl. Phys.* **2001**, 89 (10), 5509–5515.
- (45) Raino, G.; Becker, M. A.; Bodnarchuk, M. I.; Mahrt, R. F.; Kovalenko, M. V.; Stoferle, T. Superfluorescence from Lead Halide Perovskite Quantum Dot Superlattices. *Nature* **2018**, *563* (7733), 671–675.
- (46) daSilva, J. C.; Smeaton, M. A.; Dunbar, T. A.; Xu, Y. Z.; Balazs, D. M.; Kourkoutis, L. F.; Hanrath, T. Mechanistic Insights into Superlattice Transformation at a Single Nanocrystal Level Using Nanobeam Electron Diffraction. *Nano Lett.* **2020**, *20* (7), 5267–5274.
- (47) Zhu, H.; Nagaoka, Y.; Hills-Kimball, K.; Tan, R.; Yu, L.; Fang, Y.; Wang, K.; Li, R.; Wang, Z.; Chen, O. Pressure-Enabled Synthesis of Hetero-Dimers and Hetero-Rods through Intraparticle Coalescence and Interparticle Fusion of Quantum-Dot-Au Satellite Nanocrystals. *J. Am. Chem. Soc.* 2017, 139 (25), 8408–8411.
- (48) Dutta, S. K.; Mehetor, S. K.; Pradhan, N. Metal Semiconductor Heterostructures for Photocatalytic Conversion of Light Energy. *J. Phys. Chem. Lett.* **2015**, *6* (6), 936–944.
- (49) Sun, Y.; Wang, Y.; Zhu, H.; Jin, N.; Mohammad, A.; Biyikli, N.; Chen, O.; Chen, K.; Zhao, J. Excitation Wavelength-Dependent Photoluminescence Decay of Single Quantum Dots near Plasmonic Gold Nanoparticles. *J. Chem. Phys.* **2022**, *156*, 254701.
- (50) Casaletto, M. P.; Longo, A.; Martorana, A.; Prestianni, A.; Venezia, A. M. Xps Study of Supported Gold Catalysts: The Role of Au-0 and Au+Delta Species as Active Sites. *Surf. Interface Anal.* **2006**, 38 (4), 215–218.
- (51) Figuerola, A.; van Huis, M.; Zanella, M.; Genovese, A.; Marras, S.; Falqui, A.; Zandbergen, H. W.; Cingolani, R.; Manna, L. Epitaxial CdSe-Au Nanocrystal Heterostructures by Thermal Annealing. *Nano Lett.* **2010**, *10* (8), 3028–3036.
- (52) Zhang, H.; Delikanli, S.; Qin, Y.; He, S.; Swihart, M.; Zeng, H. Synthesis of Monodisperse CdS Nanorods Catalyzed by Au Nanoparticles. *Nano Res.* **2008**, *1* (10), 314–320.
- (53) Williams, D. B.; Carter, C. B. Transmission Electron Microscopy: A Textbook for Materials Science, 2nd ed.; Springer: 2008.
- (54) Zeng, J.; Huang, J. L.; Liu, C.; Wu, C. H.; Lin, Y.; Wang, X. P.; Zhang, S. Y.; Hou, J. G.; Xia, Y. N. Gold-Based Hybrid Nanocrystals through Heterogeneous Nucleation and Growth. *Adv. Mater.* **2010**, 22 (17), 1936–1940.

- (55) Sluis, P. v. d. Determination of Strain in Epitaxial Semi-conductor Layers by High-Resolution X-Ray Diffraction. *J. Phys. D: Appl. Phys.* **1993**, 26 (4A), A188–A191.
- (56) Schreiber, F. Organic Molecular Beam Deposition: Growth Studies Beyond the First Monolayer. *Phys. Status Solidi* **2004**, 201 (6), 1037–1054.
- (57) Qin, Z.; Kobayashi, M.; Yoshikawa, A. X-Ray Diffraction Reciprocal Space and Pole Figure Characterization of Cubic GaN Epitaxial Layers Grown on (001) GaAs by Molecular Beam Epitaxy. *J. Mater. Sci. Mater.* 1999, 10 (3), 199–202.
- (58) Maier, A.; Lapkin, D.; Mukharamova, N.; Frech, P.; Assalauova, D.; Ignatenko, A.; Khubbutdinov, R.; Lazarev, S.; Sprung, M.; Laible, F.; Löffler, R.; Previdi, N.; Bräuer, A.; Günkel, T.; Fleischer, M.; Schreiber, F.; Vartanyants, I. A.; Scheele, M. Structure-Transport Correlation Reveals Anisotropic Charge Transport in Coupled PbS Nanocrystal Superlattices. *Adv. Mater.* **2020**, 32 (36), 2002254.
- (59) Zaluzhnyy, I. A.; Kurta, R. P.; Andre, A.; Gorobtsov, O. Y.; Rose, M.; Skopintsev, P.; Besedin, I.; Zozulya, A. V.; Sprung, M.; Schreiber, F.; Vartanyants, I. A.; Scheele, M. Quantifying Angular Correlations between the Atomic Lattice and the Superlattice of Nanocrystals Assembled with Directional Linking. *Nano Lett.* **2017**, 17 (6), 3511–3517.
- (60) Fan, Z.; Grunwald, M. Orientational Order in Self-Assembled Nanocrystal Superlattices. *J. Am. Chem. Soc.* **2019**, *141* (5), 1980–1988.
- (61) Chen, O.; Zhao, J.; Chauhan, V. P.; Cui, J.; Wong, C.; Harris, D. K.; Wei, H.; Han, H. S.; Fukumura, D.; Jain, R. K.; Bawendi, M. G. Compact High-Quality CdSe-CdS Core-Shell Nanocrystals with Narrow Emission Linewidths and Suppressed Blinking. *Nat. Mater.* 2013, 12 (5), 445–451.
- (62) Mokari, T.; Sztrum, C. G.; Salant, A.; Rabani, E.; Banin, U. Formation of Asymmetric One-Sided Metal-Tipped Semiconductor Nanocrystal Dots and Rods. *Nat. Mater.* **2005**, *4* (11), 855–863.

□ Recommended by ACS

Real-Time Electron Microscopy of Nanocrystal Synthesis, Transformations, and Self-Assembly in Solution

Peter Sutter and Eli Sutter

DECEMBER 14, 2020

ACCOUNTS OF CHEMICAL RESEARCH

READ 🗹

Shape-Controlled Self-Assembly of Truncated Octahedral Nanocrystals into Supracrystals

Caikun Cheng, Zhijie Yang, et al.

NOVEMBER 24, 2021

THE JOURNAL OF PHYSICAL CHEMISTRY C

READ 🗹

Self-Assembly of Colloidal Nanocrystals into 3D Binary Mesocrystals

Bing Ni, Helmut Cölfen, et al.

JUNE 09, 2022

ACCOUNTS OF CHEMICAL RESEARCH

READ [7

Understanding and Controlling the Crystallization Process in Reconfigurable Plasmonic Superlattices

Maciej Bagiński, Wiktor Lewandowski, et al.

FEBRUARY 23, 2021

ACS NANO

READ 🗹

Get More Suggestions >